SIRT-TV 3D image reconstruction for a simulated muon tomography of the QinShiHuang tomb*

Ning Su,[1,2,3,4] Yuan-Yuan Liu,[1,2,3,4,†] Li Wang,[1,2,3,‡] Jian-Jie Zhang,[2] Zhi Zhou,[1,2,3,4] Xin Zhao,[1,2,3,4] Wen-Wan Ding,[1,2,3,4] Peng Zheng,[1,2,3,4] and Jian-Ping Cheng[1,2,3,4]

[1]*School of Physics and Astronomy, Beijing Normal University, Beijing, 100875, China*
[2]*Joint Laboratory of Jinping Ultra-low Radiation Background Measurement of Ministry of Ecology and Environment Beijing Normal University, 100875, China*
[3]*Jinping Deep Underground Frontier Science and Dark Matter Key Laboratory of Sichuan Province, 615000, China*
[4]*Key Laboratory of Beam Technology of Ministry of Education, 100875, China*

Cosmic-ray muons are suitable for non-destructive imaging of large-scale objects. However, due to the low statistics of cosmic-ray muons and the complicated surroundings of transmission muography experiments, transmission muography often faces challenges such as noise and incomplete data, posing certain difficulties for 3D image reconstruction. This paper applies the SIRT-TV algorithm to muon tomography, conducting a 3D image reconstruction simulation study based on a QinShiHuang tomb phantom. The results indicate that compared to the conventional SIRT algorithm, the SIRT-TV algorithm can effectively suppress artifacts in the reconstructed image, allowing for a more accurate reconstruction of the underground palace. The geometric similarity of the walls reconstructed by SIRT-TV is nearly tripled compared to that of SIRT. This study also discusses the impact of TV-minimization algorithm parameters, and the measurement configurations and durations on the quality of the reconstructed image, providing a reference point for future experiments.

Keywords: Muography, Monte Carlo simulation, Image reconstruction

I. INTRODUCTION

Transmission muography, utilizing naturally existing cosmic-ray muons, images the internal structures of the objects penetrated by muons. Due to their high average energy (4 GeV at sea level [1]), cosmic-ray muons have strong penetrating power and nearly straight-line trajectories. Additionally, they are ubiquitous surrounding the earth. These characteristics make cosmic-ray muons particularly suitable for non-destructive imaging of large-scale objects, such as volcanoes [2–4], faults [5–7], mineral deposits [8–11], cultural heritage [12–16], and nuclear reactors [17–19].

The flux attenuation due to energy loss of muons interacting with matter is related both to the thickness and density of the material penetrated by the muons. By analyzing cosmic-ray muon flux detected from a single view and combining it with prior topographic information, the average density of the object along the line of sight can be obtained, allowing for the identification of density anomalies within the object. This kind of 2D transmission muography is called "muon radiography". However, muon radiography has a limitation: the resulting density map is only a 2D projection. This would introduce more ambiguities when the internal structure of the object is complex, say, the density anomalies may overlap along the measurement direction. In such cases, the overlapping structures in the image obtained by muon radiography are degenerate. To alleviate this ambiguity, it is helpful to obtain 3D information of the object's internal structure. At least two different views of cosmic-ray muon flux measurements are required to locate the 3D coordinates of density anomalies. For example, in the ScanPyramids experiment of the Khufu Pyramid in 2017 [12], three sets of independent muon measurements were conducted. Each set of measurements were taken from two different positions so as to locate the hidden chamber with a triangulation analysis. The positions located by the three independent analyses agree with one another, thus confirming this discovery with high confidence. With muon flux data obtained from multiple views, it is possible to reconstruct the 3D density distribution of an object. This kind of 3D transmission muography is called "muon tomography".

Constrained by the characteristics of cosmic-ray muons, muon tomography faces two major challenges. First, due to the relatively low flux of cosmic-ray muons, which is around $1\,\mathrm{cm^{-2}\cdot min^{-1}}$ at sea level [1], the number of views is limited both by experimental time and the availability of muon detectors. Additionally, the choice of detector sites is constrained, given that the structure under test in transmission muography is often a large-scale object located in the field and the surroundings are complicated. Consequently, the problem of image reconstruction in muon tomography is often underconstrained, potentially leading to ambiguity results. Second, fluctuations in the cosmic-ray muon flux data can disturb the image reconstruction in muon tomography, including statistical fluctuations caused by the low statistics of cosmic-ray muons and directional fluctuations caused by multiple Coulomb scattering of muons penetrating objects [20].

To address the two challenges mentioned above, efforts can be made from two perspectives: combining cosmic-ray muon data with other types of geophysical data for joint inversion, and improving image reconstruction algorithms. From the perspective of joint inversion, both transmission muography and gravimetry are sensitive to the density of objects, making them naturally suitable for joint inversion; thus, muon data are often combined with gravity data for such inversions. Several studies have reported on the inversion results com-

* Supported by the National Natural Science Foundation of China (No. 12222502).
† Corresponding author, E-mail: yyliu@bnu.edu.cn
‡ Corresponding author, E-mail: wangl@bnu.edu.cn

bining cosmic-ray muon data with gravity data. For instance, R. Nishiyama et al. combined single-view cosmic-ray muon data with gravity data obtained from 30 gravity stations to reconstruct the 3D density structure of the Showa-Shinzan lava dome. They also demonstrated through the inversion of synthesized data that the results of joint inversion using both gravity and cosmic-ray muon data had better resolution than those using only gravity data [21]. However, K. Jourde et al. noted in their study that when the object is covered by cosmic-ray muon data from more than two viewpoints, the improvement in image quality from adding gravity data is insignificant [22].

From the perspective of enhancing image reconstruction algorithms, it is important to establish robust algorithms with strong noise resistance, giving that the 3D image reconstruction problem in muon tomography involves reconstructing images from noisy and incomplete data. Currently, the algorithms used for 3D image reconstruction in muon tomography can be divided into two main categories. The first category is the linear inversion method based on Bayesian principles, which is widely used in the inversion of geophysical models. This method can be applied to the inversion of muon tomography. As an example, Shogo Nagahara et al. used linear inversion to reconstruct the 3D density distribution of the Omuroyama scoria cone from cosmic-ray muon data obtained from 10 viewpoints [23]. This method can also be used for the joint inversion of gravity data and cosmic-ray muon data, as demonstrated by Anne Barnoud et al., who used linear inversion to reconstruct the 3D density structure of the Puy de Dôme volcano, using the joint inversion of single-view cosmic-ray muon data and gravimetric data acquired from 650 measurement points [24]. However, this method involves multiple a priori parameters, and the selection of these parameters directly affects the inversion results, so they need to be tuned carefully. Additionally, the density smoothing constraint used in the inversion may blur the boundaries of density anomaly regions [25]. The second category is algebraic reconstruction techniques, which are widely used in medical CT image reconstruction and are suitable for image reconstruction with incomplete and noisy data. Many studies have applied algebraic reconstruction techniques to muon tomography. Erlandson et al. simulated cosmic-ray muons passing through the ZED-2 research reactor, and conducted muon tomography reconstruction using the ART (Algebraic Reconstruction Technique) algorithm [26]. S. Procureur used the SART (Simultaneous ART) algorithm to reconstruct the image for the simulated muon tomography of a concrete cube with cavities [27]. K. Hartling et al. simulated a 12-view muon tomography for a cylindrical model containing a uranium rod and compared various iterative reconstruction algorithms, concluding that the SIRT (Simultaneous Iterative Reconstruction Technique) is a suitable algorithm for muon tomography reconstruction [28]. Compared to the classic ART algorithm, the SIRT algorithm can better suppress noise.

Additional information can be incorporated into the SIRT algorithm to further improve the reconstructed image quality. One very effective constraint is total-variation (TV) minimization. It is demonstrated that signals or images that have transform sparsity can be accurately reconstructed from a small number of samples by minimizing the L1-Norm of the transform coefficients [29–31]. For piecewise constant images, their gradient-magnitude images meet the transform sparsity condition, and TV is the L1-Norm of gradient-magnitude image. Therefore, TV-minimization-based image reconstruction algorithms may achieve high-precision reconstruction from a limited number of views [32, 33]. The density distribution of large cultural heritage structures, such as the Khufu Pyramid, is piecewise constant, making them suitable for TV-minimization. Therefore, combining SIRT with TV-minimization could potentially enhance the image quality of muon tomography reconstruction for such cases.

In 2022, our group reported on the preliminary results of a cultural heritage muon radiography simulation study based on the archaeological data of the QinShiHuang tomb. The study demonstrated that muon radiography could identify the inner structures of the underground palace, including the tomb chamber, walls, and rammed earth. From the muon radiography simulation results obtained from two viewpoints, the length, width, and burial depth of the tomb chamber were estimated [34]. Based on the previous research, this paper carries out 3D image reconstruction for the muon tomography of QinShiHuang tomb. A digital phantom, built based on the archaeological data of the QinShiHuang tomb, is used for transmission muography simulation in Geant4, and to test the image reconstruction algorithm. The SIRT-TV algorithm, which combines SIRT and TV-minimization, is applied to the image reconstruction of a 12-view muon tomography. This paper is organized as follows: Section II of the paper introduces the principles of transmission muography and the SIRT-TV algorithm. Section III describes the simulation setup, and presents the 2D slices of reconstructed images using the SIRT-TV and the SIRT algorithms. The slices reconstructed with the two algorithms, under the same number of iterations, are compared visually. Section IV evaluates the reconstructed image quality based on the geometry similarity index for structures of the underground palace, providing a quantitative comparison of SIRT and SIRT-TV. This section also discusses some factors that may influence the reconstructed image quality, including the value of TV-minimization algorithm parameters, the number of views in muon tomography, and the statistics of muon data. The final section concludes this paper.

II. METHODS

A. Principles of muon radiography

Muons, while passing through an object, interact with matter and lose energy through ionization, bremsstrahlung, pair production, and photonuclear reactions. The energy loss behavior can generally be described as:

$$-\frac{\mathrm{d}E}{\mathrm{d}X} = a + bE, \tag{1}$$

where a represents the ionization term, b is the sum of the other three radiation loss terms. Both a and b depend on the

muon's energy and the composition of the material. Their values can be obtained from the tables provided by the Groom et al [35]. $X = \int \rho \mathrm{d}l$ is the integral of the object's density along the muon's path, referred to as the object's density length. If a muon with energy $E_{\min}$ loses all its energy after penetrating an object with density length X_1, then X_1 can be expressed as,

$$X_1 = \int_{E_\mu}^{E_{\min}} -\frac{\mathrm{d}X}{\mathrm{d}E}\mathrm{d}E, \tag{2}$$

where E_μ is the rest mass of the muon. Combining Eqs. (1) and (2), the value of X_1 can be numerically calculated. Alternatively, Monte Carlo simulations can be used to determine the maximum density length that muons of different energies can penetrate. By fitting the simulation results, a fitted formula that describes the relationship between X_1 and $E_{\min}$ can be obtained. $E_{\min}$ can be determined from the measured cosmic-ray muon flux I, which can be expressed as the integral of the differential energy spectrum $\phi(E)$:

$$I = \int_{E_{\min}}^{+\infty} \phi(E)\mathrm{d}E. \tag{3}$$

Unlike traditional imaging techniques that use artificial radiation sources, transmission muography uses naturally existing radiation sources whose energy spectrum $\phi(E)$ cannot be manually modulated. Moreover, since the targets in transmission muography experiments are usually large, it is impractical to use detectors to measure the cosmic-ray muon energy spectrum $\phi(E)$ in real-time before the muons penetrate the target. Nonetheless, theoretical studies and experimental measurements show that the sea-level cosmic-ray muon energy spectrum is relatively stable and can be reliably modeled. The angular distribution of sea-level cosmic-ray muons is roughly $\propto \cos^2\theta$, where θ is the zenith angle of the cosmic-ray muons. Their energy spectrum nearly follows a power law with a negative exponent. Therefore, the transmitted muon flux mainly consists of muons with energy near $E_{\min}$. Classic formulas such as Gaisser/Tang and Reyna are commonly used to describe the cosmic-ray muon energy spectrum at sea level, as they provide reliable descriptions in the energy range most relevant to transmission muography [36].

Combining Eqs. (1)–(3) and the sea-level cosmic-ray muon energy spectrum model, the density length of the object in different directions can be obtained, resulting in a 2D projection map of the object's density length X.

B. 3D image reconstruction of muon tomography

Based on the 2D projection map of X obtained in Section II A, the 3D density distribution can be solved for. Let m denote the number of directions. Dividing the 3D region of interest (ROI) uniformly into n voxels, the integral $X = \int \rho \mathrm{d}l$ can be discretized as:

$$x_i = \sum_{j=1}^{n} l_{i,j}\rho_j, i = 1, \cdots, m, \tag{4}$$

where x_i represents the density length along the i-th ray, ρ_j represents the density of the j-th voxel, and $l_{i,j}$represents the intersection length of the i-th ray within the j-th voxel. The relationship between the density lengths along different directions and the density distribution can be expressed as a system of linear equations:

$$\boldsymbol{X} = \boldsymbol{L}\boldsymbol{\rho}, \tag{5}$$

where $\boldsymbol{X} = (x_1, x_2, \cdots, x_m)^T$ represents the density lengths of the object along different directions, $\boldsymbol{L} = \{l_{i,j}\}$ represents the intersection length of rays within the voxels along different directions, and $\boldsymbol{\rho} = (\rho_1, \rho_2, \cdots, \rho_n)^T$ represents the densities of the voxels.

Since the density length data is obtained from the cosmic-ray muon flux data, which is usually noisy and incomplete, the linear equations in Eq. (5) face issues such as being underdetermined and inconsistent, and having a large sparse system matrix. Algebraic reconstruction techniques are commonly used methods for solving such problems. The most basic algorithm in algebraic reconstruction techniques is the ART algorithm [37], which is based on the Kaczmarz optimization algorithm. The principle of ART can be understood as gradually projecting the trial solution onto the hyperplanes determined by each equation to obtain a new solution. If the system of equations has a unique solution, the trial solution will iteratively converge to that solution. In every iteration of the ART algorithm, each equation of Eq. (5) updates $\boldsymbol{\rho}$ once. This equation-by-equation update method is sensitive to noise and can even cause divergence if the noise is severe. To suppress the noise, the SIRT algorithm was developed based on the basic ART algorithm [38]. In one iteration of the SIRT algorithm, the contribution of each equation to $\boldsymbol{\rho}$ is first calculated without updating $\boldsymbol{\rho}$. After going through all the equations, the contributions of all the equations are averaged and then $\boldsymbol{\rho}$ is updated accordingly. The update equation of SIRT is:

$$\rho^k_{\mathrm{SIRT},j} = \rho^{k-1}_{\mathrm{SIRT},j} + \lambda \frac{\sum_{i=1}^m L_{i,j} \frac{X_i - \boldsymbol{L}_i \boldsymbol{\rho}^{k-1}}{\sum_{j=1}^n L_{i,j}}}{\sum_{i=1}^m L_{i,j}}, \tag{6}$$

where k represents the number of iterations, and λ is used to control the iteration step size and is usually set to 1.

Both ART and SIRT solve the reconstruction problem solely based on the projection data $\boldsymbol{X}$, without introducing any additional constraints. However, muon tomography often lacks sufficient views, resulting in the ill-posedness of the image reconstruction. To further improve the quality of reconstructed image, it is necessary to introduce additional constraints to the reconstruction procedure. We observe that the density distribution of the targets in muon tomography typically exhibits piecewise constancy, meaning its gradient magnitude image is sparse. This makes it suitable to use TV-minimization as a constraint.

Let the voxel density at coordinates (r, s, t) be $\rho_{r,s,t}$. Then, the total variation of the density image is:

$$\begin{aligned}\|\boldsymbol{\rho}\|_{\mathrm{TV}} &= \sum_{r,s,t} |\nabla \rho_{r,s,t}| \\ &= \sum_{r,s,t} \sqrt{\left(\rho_{r,s,t}-\rho_{r-1,s,t}\right)^2 + \left(\rho_{r,s,t}-\rho_{r,s-1,t}\right)^2 + \left(\rho_{r,s,t}-\rho_{r,s,t-1}\right)^2}.\end{aligned} \tag{7}$$

Using the gradient descent algorithm to solve the TV-minimization problem, let

$$\boldsymbol{\rho}_{\mathrm{TV}}^{0} = \boldsymbol{\rho}_{\mathrm{SIRT}}^{k}, \tag{8}$$

$$d\rho = \|\boldsymbol{\rho}_{\mathrm{SIRT}}^{k} - \boldsymbol{\rho}_{\mathrm{SIRT}}^{k-1}\|_2, \tag{9}$$

$$\vec{\boldsymbol{v}}^{k'} = \nabla_{\rho} \|\boldsymbol{\rho}_{\mathrm{TV}}^{k'}\|_{\mathrm{TV}}, \tag{10}$$

and

$$\hat{\boldsymbol{v}}^{k'} = \vec{\boldsymbol{v}}^{k'} / |\vec{\boldsymbol{v}}^{k'}|, \tag{11}$$

for $k' = 1, 2, \cdots, N_{\mathrm{TV}}$, do TV gradient descent:

$$\boldsymbol{\rho}_{\mathrm{TV}}^{k'} = \boldsymbol{\rho}_{\mathrm{TV}}^{k'-1} - \alpha \cdot d\rho \cdot \hat{\boldsymbol{v}}^{k'-1}. \tag{12}$$

where α controls the TV gradient descent step size, and the total number of gradient descent iterations is controlled by N_{TV}. In Ref. [32] TV-minimization is combined with ART, but considering that data noise is more significant in muon tomography, this paper opts to combine SIRT with TV-minimization for image reconstruction. The SIRT-TV procedure terminates when the number of iterations reaches $N_{\max}$. The overall process of muon tomography image reconstruction in this work is shown in Fig. 1. Note that after the SIRT-step in each iteration k, a non-negative constraint is applied to $\boldsymbol{\rho}_{\mathrm{SIRT}}^{k}$. Any additional prior information about $\boldsymbol{\rho}$ can also be incorporated at this step.

III. SIMULATION AND RECONSTRUCTION

A. Muography simulation

The simulation is performed using Geant4, a Monte Carlo toolkit developed by CERN based on C++ [39]. Geant4 can simulate the transport and interactions of particles in matter, and is a commonly used and reliable simulation platform for transmission muography. The simulation model can be divided into three parts: the QinShiHuang tomb phantom, the muon track detector, and the cosmic-ray muon source.

The QinShiHuang tomb has been studied using 20 geophysical approaches as part of the national 863 Hi-tech project. The archaeological results confirmed the depth of the underground palace, as well as the size and location of the tomb chamber and the surrounding walls [40]. Based on these archaeological data, we built a phantom model of the QinShiHuang tomb in our simulation, which includes the mound, rammed earth, loam wall, stone wall, burial chamber, and surrounding land, as shown in Fig. 2.

The cosmic-ray muon source is sampled with the Reyna formula [41]:

$$\phi(p,\theta) = c_1 \cos^3\theta (p^*)^{-[c_2 + c_3 \log_{10}(p^*) + c_4 \log_{10}^2(p^*) + c_5 \log_{10}^3(p^*)]}, \tag{13}$$

where θ is the zenith angle of cosmic-ray muons, p is the momentum of cosmic-ray muons in GeV/c, $p^* = p\cos\theta$, $c_1 = 0.00253$, $c_2 = 0.2455$, $c_3 = 1.288$, $c_4 = -0.2555$, and $c_5 = 0.0209$. This formula is suggested for a momentum range of $1\ \mathrm{GeV/c} < p < 2000/\cos\theta\ \mathrm{GeV/c}$ and a zenith angle range of $0^\circ \le \theta \le 90^\circ$.

The coordinate system is defined as shown in Fig. 2(b-d). The muon track detector is set as a $1\ \mathrm{m} \times 1\ \mathrm{m}$ ideal detector placed horizontally, recording the direction of cosmic-ray muons passing through it. To avoid interfering with the structure of the underground palace, the selected detector positions are $5\ \mathrm{m}$ away from the boundaries of the underground palace. 12 detector locations are selected, evenly spaced at an angle of 30° surrounding the center of the underground palace, numbered 1 to 12, as shown in Fig. 2(b). Since the incident directions of the cosmic-ray muons are always downward, detectors must be positioned lower than the underground palace to ensure that their field of view can fully cover the ROI. It is important to select a suitable depth for the detector, as the angular size of the ROI, the thickness of the overburden above the detector, and the zenith angle of the detected muons traversing the ROI all come into play. We set the detectors' burial depth to $90\ \mathrm{m}$, as shown in Fig. 2(c). At this depth, the maximum zenith angle of the detected muons crossing the ROI is no more than 75°. To reduce simulation time, we referred to the method in Reference [42] to determine the minimum energy of muons that can penetrate the phantom and reach the detector. Only muons with energy exceeding this minimum energy are sampled. The simulated cosmic-ray muon statistics for a single view are equivalent to a 180-day physical measurement.

B. Image reconstruction

Since the tomb phantom is much larger than the detectors, the detectors are treated as points for the calculation of muon flux and density length maps. The simulated cosmic-ray muon fluxes after penetrating the QinShiHuang tomb phantom, as detected by each detector, are divided into 75×180 directions, according to their zenith and azimuth angles, as shown in Fig. 3. The direction of each pixel in Fig. 3 is represented by its center coordinate. The minimum energy $E_{\min}$ of cosmic-ray muons penetrating the phantom can be calculated

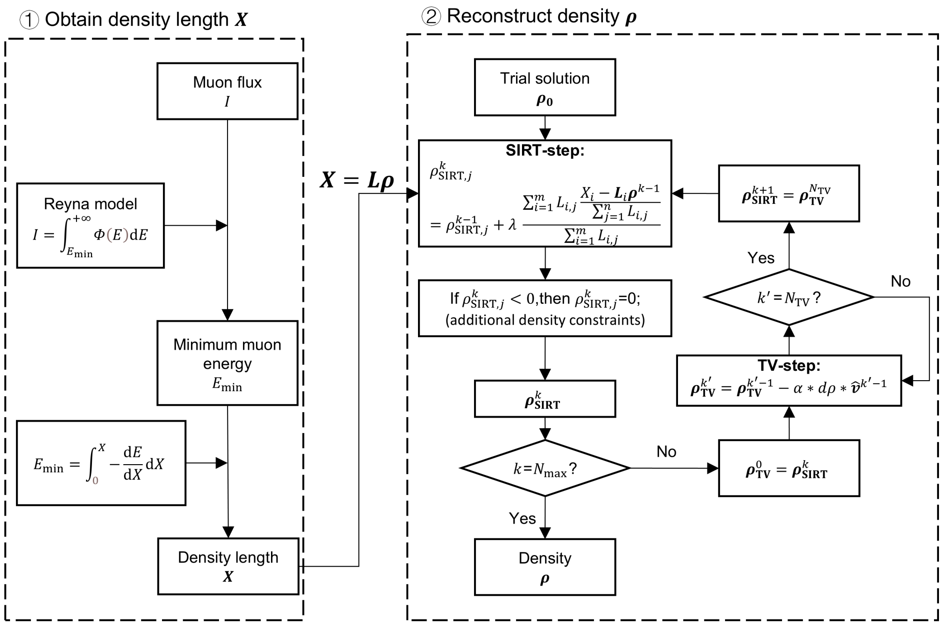

Fig. 1. Flowchart of muon tomography image reconstruction using the SIRT-TV algorithm.

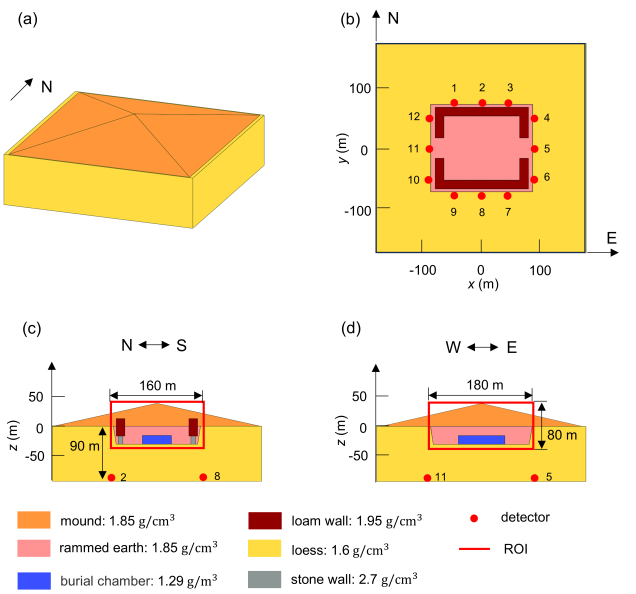

Fig. 2. Schematic of the QinShiHuang tomb phantom. (a) 3D view of the phantom. (b) Cross-section view of the phantom at $z = 0$, with red dots indicating the projections of the detector positions on the cross-section. (c) Cross-section view of the phantom at $x = 0$. (d) Cross-section view of the phantom at $y = 0$. The rectangles in (c) and (d) represent the ROI for 3D image reconstruction.

using Eq. (3). For the conversion to the density length, this paper uses Geant4 to simulate the average penetration range of muons with different energies in loess, with the simulation results shown in Fig. 4. A second-order polynomial is fitted to the curve in Fig. 4.

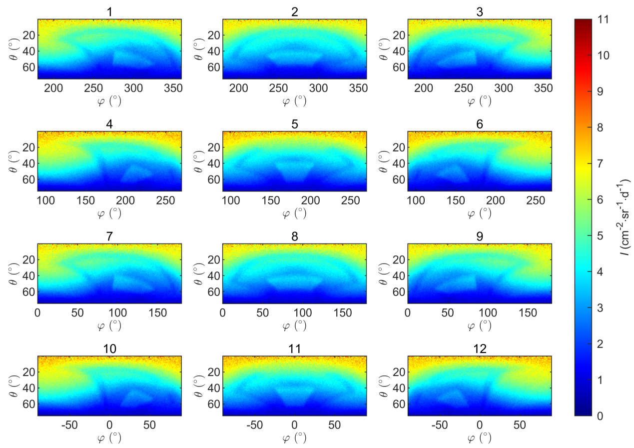

Fig. 3. Simulated cosmic-ray muon fluxes penetrating the QinShi-Huang tomb phantom, measured by 12 detectors using Geant4. The numbers above the figures correspond to the detector IDs in Fig. 2. θ and φ represent the zenith and azimuth angles of the incident muons in the horizontal coordinate system.

Since we are primarily interested in the structure of the underground palace, we define the ROI as shown in Fig. 2(c) and 2(d) and perform 3D image reconstruction only for the density distribution within the ROI. The density length data obtained from different directions in the simulation include contributions from both inside and outside the ROI. For the tomb phantom, the density distribution outside the ROI is

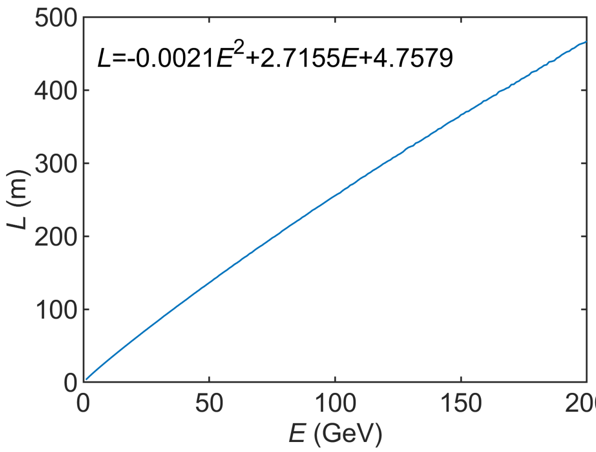

Fig. 4. The average penetration range of muons in loess as a function of muon energy obtained from Geant4 simulations.

known, allowing us to directly calculate the density length outside the ROI. By subtracting the density length outside the ROI from the obtained density length data, we get the density length only within the ROI, as shown in Fig. 5. Note that some directions in the figure have negative density length values due to fluctuations in cosmic-ray muon flux. Only non-negative density length values are used in the image reconstruction process.

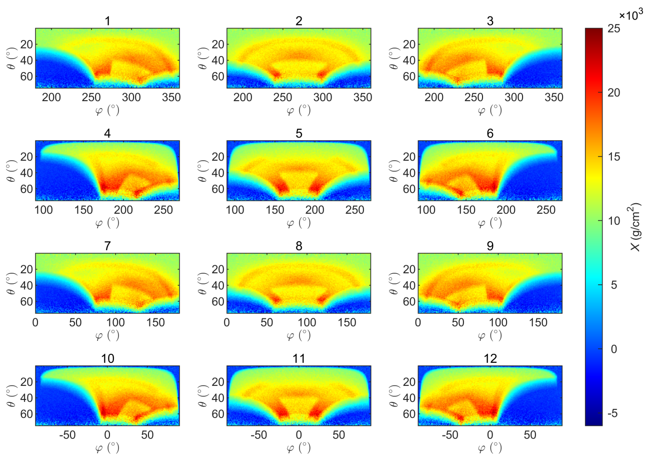

Fig. 5. Density length maps of the tomb phantom ROI converted from the 12-view simulated muon fluxes.

In 3D image reconstruction, the ROI is divided into $60 \times 50 \times 20$ voxels, resulting in a voxel size of $3\,\mathrm{m} \times 3.2\,\mathrm{m} \times 4\,\mathrm{m}$. This voxelization ensures that the number of voxels will not be too large to solve the linear equations in Eq. (5), and that the voxel size will not be too large to reconstruct the fine structures in the underground palace. Both SIRT and SIRT-TV are used to reconstruct images from the same density length data, so as to compare their reconstruction results. Following the parameter values from Ref. [32], we set $\lambda = 1$, $\alpha = 0.2$, and $N_{\mathrm{TV}} = 20$. The initial density values for iteration are set to $\boldsymbol{\rho}_0 = 1.6\ \mathrm{g/cm^3}$, which are the same as the loess density in the phantom. Both algorithms are iterated $N_{\max} = 50$ times. An additional constraint is incorporated into each iteration of the algorithms introduced in Section II B, restricting the voxel density outside the burial mound to $0.00129\ \mathrm{g/cm^3}$, which is the same as the air density in the phantom. Slices of the reconstructed images at three representative locations are selected for comparison with the phantom slices, as shown in Fig. 6.

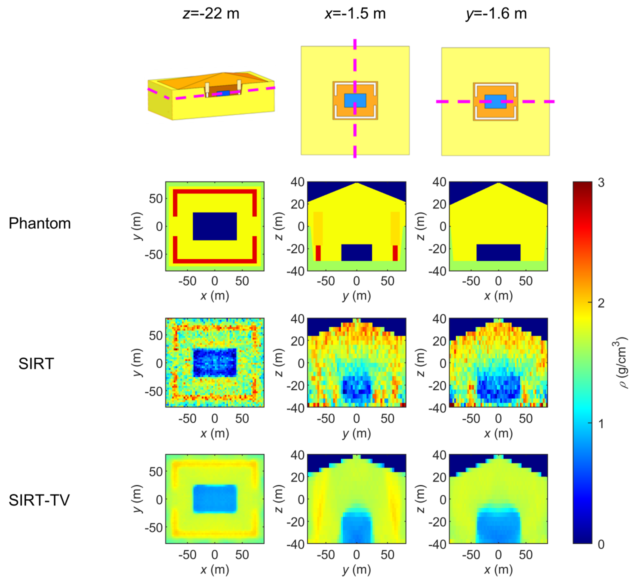

Fig. 6. Comparison of the slices of 3D density distribution between the phantom and the reconstruction results of SIRT and SIRT-TV. The dashed lines indicate the locations of the slices.

Comparing the slices of the reconstructed images obtained by the two algorithms with those of the phantom, it can be observed that the shapes and positions of the tomb chamber and walls in the SIRT-TV reconstruction result match the phantom. In contrast, the slices obtained using the SIRT algorithm exhibit significant salt-and-pepper artifacts, particularly notable at the bottom of the reconstructed image, around the tomb chamber, and at the top of the burial mound. These artifacts could potentially lead to misinterpretations of the underground palace's structure. The reconstruction result obtained using SIRT-TV does not show such significant artifacts, preliminarily verifying that the inclusion of TV-minimization can effectively suppress artifacts.

IV. DISCUSSION

A. Reconstructed image quality assessment

In Fig. 6, a visual comparison of the reconstructed images using SIRT and SIRT-TV is presented. However, the visual comparison lacks quantitative information and is noncompre-

hensive since the reconstructed images are 3D. To quantitatively compare the reconstruction results of SIRT and SIRT-TV, it is necessary to use appropriate image quality assessment metrics. Classic metrics include mean squared error (MSE), peak signal-to-noise ratio (PSNR), and structural similarity (SSIM) [43]. These metrics can evaluate the overall similarity between the reconstructed image and the phantom. However, in this study, we are more concerned with whether the structures of the underground palace, namely the tomb chamber and walls, can be properly reconstructed. Referring to the image quality assessment metrics used in Ref. [28], we use the Jaccard similarity index J to assess the geometric similarity of the reconstructed images to the phantom for the tomb chamber and walls. The definition of J is given by:

$$J(P,R) = \frac{|P \cap R|}{|P \cup R|}, \tag{14}$$

where P represents the set of voxels belonging in the tomb chamber or walls in the phantom, and R represents the set of voxels belonging in the same structure in the reconstructed image. The term $|P \cap R|$ denotes the number of elements in the intersection of P and R, while $|P \cup R|$ denotes the number of elements in the union of P and R. A larger $J(P,R)$ indicates a higher geometric similarity, and when $J(P,R) = 1$, it signifies that the geometric structures of the phantom and the reconstructed image are identical. When calculating $J(P,R)$ for the reconstructed images in Section III, we face the issue of inconsistent voxel segmentation between the phantom and the reconstructed images, since the phantom established in Geant4 is not voxelized. To address this problem, we modify Eq. (14). We define a vector $\boldsymbol{p}$ representing the proportion of overlap between the voxels defined in the reconstructed images and the corresponding structure in the phantom. Consequently, the element p_i corresponding to the i-th voxel can take on three types of values:

$$p_i = \begin{cases} 0 & \text{voxel outside the corresponding structure,} \\ 1 & \text{voxel inside the corresponding structure,} \\ q & \text{voxel partially overlaps with the corresponding} \\ & \text{structure with a proportion of } q. \end{cases} \tag{15}$$

Define a vector $\boldsymbol{r}$ to represent whether each voxel belongs in the structure in the reconstructed image. The element r_i corresponding to the i-th voxel can take on two values:

$$r_i = \begin{cases} 0 & \text{voxel outside the corresponding structure,} \\ 1 & \text{voxel inside the corresponding structure.} \end{cases} \tag{16}$$

Therefore, Eq. (14) can be redefined as:

$$J(\boldsymbol{p},\boldsymbol{r}) = \frac{\sum_{i=1}^{n} p_i \cdot r_i}{\sum_{i=1}^{n} p_i + \sum_{i=1}^{n} r_i - \sum_{i=1}^{n} p_i \cdot r_i}. \tag{17}$$

In the phantom established in this study, there are partial overlaps between the voxels and the corresponding structure, so the maximum value of $J(\boldsymbol{p},\boldsymbol{r})$ cannot reach 1. When calculating $\boldsymbol{r}$, image segmentation is necessary to extract the tomb chamber and walls structures from the reconstructed images. Since the density of the tomb chamber and the density of the walls correspond to the minimum and maximum densities in the phantom, respectively, image segmentation can be performed using density thresholds for these two structures. The structures are extracted based on whether the voxel density values fall within the specified density ranges. For the tomb chamber:

$$r_i^{\text{chamber}} = 1, \text{if } \rho_i < \text{threshold of chamber and } z < 0. \tag{18}$$

And for the walls:

$$r_i^{\text{wall}} = 1, \text{if } \rho_i > \text{threshold of wall.} \tag{19}$$

Ideally, the thresholds should be set according to the density values of the structures in the phantom. However, due to the differences between the densities in the reconstructed images and the phantom—especially since the densities of the tomb chamber in the reconstructed images are much higher than the density of air in the phantom—an optimization approach is used to find the most suitable threshold for image segmentation. Considering that the density of the chamber is lower than that of loess, while the density of the walls is higher than that of loess, the density threshold for the tomb chamber is searched within the range of $(0, 1.6\ \mathrm{g/cm^3}]$ and the density threshold for the walls is searched within the range of $(1.6\ \mathrm{g/cm^3}, 2.7\ \mathrm{g/cm^3}]$, with a step size of $0.1\ \mathrm{g/cm^3}$. For each density threshold, J is calculated, and the highest J is taken as the geometric similarity of the reconstructed image, denoted as J_{chamber} for the tomb chamber and J_{wall} for the walls. The thresholds are searched for the reconstructed images obtained in Section III. The voxel sets belonging in the tomb chamber and walls in the reconstructed images are extracted according to the density thresholds with the highest J, and the voxel positions obtained from image segmentation are shown in Fig. 7.

Both the wall and tomb chamber geometries in the SIRT reconstruction result show noticeable overflow compared to the phantom. In contrast, their counterparts extracted from the SIRT-TV reconstructed image align better with the phantom. Table 1 provides the J calculation results for structures in the reconstructed images obtained by the two algorithms. Both J_{chamber} and J_{wall} in the SIRT-TV reconstruction result are superior to those obtained with SIRT. Particularly, J_{wall} is 2.8 times that of SIRT.

TABLE 1. J_{chamber} and J_{wall} of the reconstructed images obtained using SIRT and SIRT-TV.

Algorithm	J_{chamber}	J_{wall}
SIRT-TV	0.5929	0.5498
SIRT	0.4611	0.1978

B. Iterative convergence

The convergence speed is an important metric for evaluating iterative image reconstruction algorithms. In Section

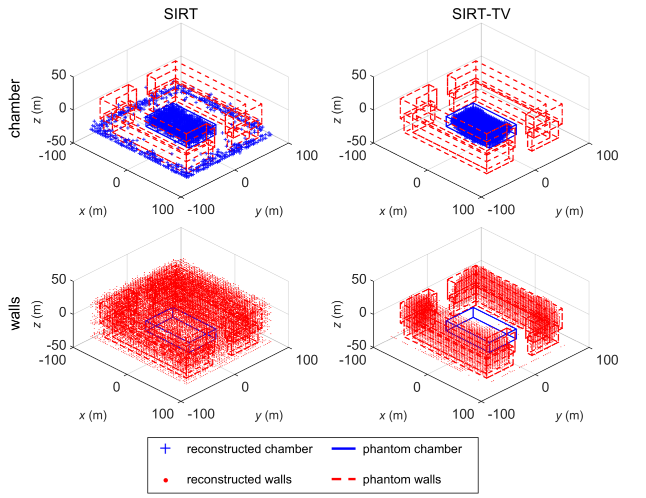

Fig. 7. Comparison between the structures extracted from reconstructed images obtained using two algorithms and the structures in the phantom, based on the best density thresholds. The blue crosses and red dots represent the voxel positions of the chamber and the walls in the reconstructed images, respectively. The blue box outlines the boundaries of the tomb chamber in the phantom, and the red box outlines the boundaries of the walls.

IV A, the J_{chamber} and J_{wall} of the reconstruction results are compared after the same number of iterations for both algorithms, but the number of iterations required for each algorithm to converge may differ. To compare the convergence speeds of the two algorithms, both algorithms were iterated 150 times, and the curves showing the changes in J_{chamber} and J_{wall} with the number of iterations are plotted in Fig. 8. The J_{chamber} and J_{wall} of SIRT-TV generally increase with the number of iterations until convergence, whereas those for SIRT initially increase but then decrease with additional iterations before convergence.

To quantitively evaluate the convergence speed, we define a convergence metric:

$$\Delta J/J = \frac{|J^{k+1} - J^{k}|}{J^{k}} < \varepsilon, \tag{20}$$

where k represents the number of iterations, and ε is the threshold for convergence. The $\Delta J/J$ values for both algorithms as functions of iterations are plotted in Fig. 8. It can be seen that $\Delta J/J$ for both algorithms fluctuate with increasing iteration numbers while converging. These fluctuations are due to the discreteness of structure thresholds and voxelization. With ε set to 0.002, J_{chamber} and J_{wall} for SIRT-TV converge after 36 and 24 iterations, respectively, whereas those of SIRT have not yet converged. This indicates that SIRT-TV reaches convergence faster than SIRT. The faster convergence of SIRT-TV is due to the effective constraint of the TV-minimization on the reconstruction procedure. For the SIRT algorithm, the convergence speeds of J_{chamber} and J_{wall} are different because of the structural differences between the tomb chamber and walls: the tomb chamber is a relatively large cubic volume, while the walls are more complex and thinner.

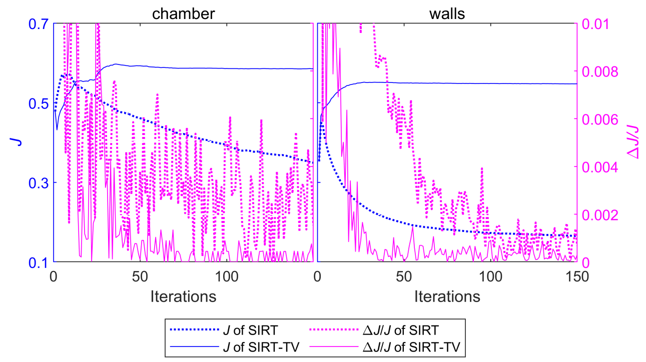

Fig. 8. J and $\Delta J/J$ of the reconstructed images obtained by SIRT and SIRT-TV as functions of iterations.

C. Impact of TV parameters on reconstruction

The values of the parameters in the TV-minimization algorithm may affect the quality of the reconstructed images. To assess this impact, we vary the maximum iteration number N_{TV} and the TV gradient descent step size α. J_{chamber} and J_{wall} as functions of iterations for different parameter values are shown in Fig. 9.

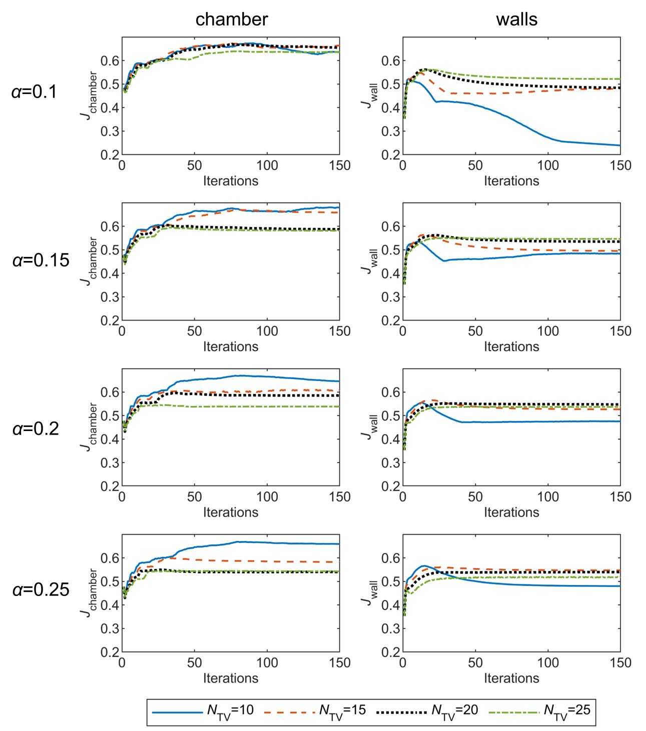

Fig. 9. J_{chamber} and J_{wall} of reconstructed images obtained under different TV parameters, as functions of iterations.

For most $(N_{\mathrm{TV}}, \alpha)$ combinations, convergence is achieved within 50 iterations, indicating that choosing a maximum iteration number $N_{\max} = 50$ as the termination criterion for SIRT-TV is reasonable. For J_{wall}, when $N_{\mathrm{TV}} = 10$ and $\alpha = 0.1$, the generally trend with increasing iterations is similar to that of SIRT, and there is still a downward trend after 150 iterations. This indicates that the TV-minimization algorithm with these parameter values does not effectively improve reconstructed image quality. With different α values, J_{wall} is always the lowest when $N_{\mathrm{TV}} = 10$. Unlike J_{wall}, for different α values (except $\alpha = 0.1$), J_{chamber} is always the highest when $N_{\mathrm{TV}} = 10$, and remains above 0.5 regardless of the parameter values. This suggests that compared to the walls, the reconstruction of the tomb chamber does not require a stringent TV constraint.

Overall, the different parameter values in Fig. 9 (except $N_{\mathrm{TV}} = 10$ or $\alpha = 0.1$) do not significantly affect the reconstruction results, indicating that the SIRT-TV algorithm can reliably produce high-quality images.

D. Impact of measurement configuration and duration

As mentioned in Section I, the main challenges in 3D reconstruction of muon tomography lie in the presence of noise and incomplete data. In Section III, to test the feasibility of the algorithm, we simulated relatively ideal conditions. This section discusses the impact of less ideal measurement configurations and durations, i.e., fewer views and lower muon statistics, on the reconstruction with SIRT-TV.

1. *Measurement configuration*

Using the same simulation data from Section III, the number of views is reduced to 4, and three different detector configurations are selected for reconstruction. The parameters of the image reconstruction algorithm remain the same as those in Section III. Fig. 10 shows the slices of the phantom, and reconstructed images for the 12-view configuration and three 4-view configurations. It can be seen that the reduction in the number of views leads to an increase in artifacts. Among these 4-view configurations, the symmetrical 4-view configuration shows better geometric symmetry in its reconstruction result, while the reconstruction results for the other two 4-view configurations exhibit distortions in the shapes of the tomb chamber and walls. The calculation results of J_{chamber} and J_{wall} in Table 2 also indicate that, among the three different 4-view configurations, the reconstructed image quality is highest for the symmetrical 4-view configuration. These artifacts can be explained by the ray densities in the voxels. Given that the voxelization for each reconstruction is the same, more views will lead to more rays, higher ray densities in the voxels, and more information about the voxel density. When voxelization and the number of views is the same for each reconstruction, asymmetrical measurement configurations will cause greater variation in ray densities across voxels. This means that some voxels will be crossed by only a few rays, making their densities difficult to reconstruct. Symmetrical measurement configuration results in better reconstruction quality.

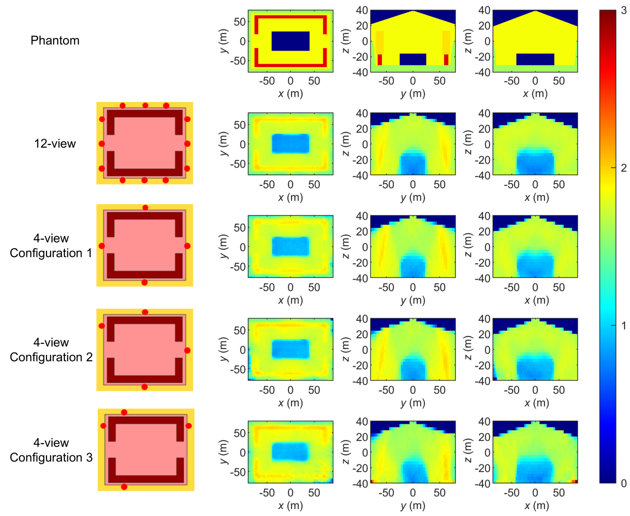

Fig. 10. Slices of the phantom, and reconstructed images for the 12-view configuration and three 4-view configurations.

TABLE 2. J_{chamber} and J_{wall} of the images obtained from the 12-view reconstruction and three 4-view reconstructions.

Measurement configuration	J_{chamber}	J_{wall}
12-view	0.5929	0.5498
4-view Configuration 1	0.5161	0.4552
4-view Configuration 2	0.4818	0.4452
4-view Configuration 3	0.4576	0.3777

2. *Measurement duration*

The number of cosmic-ray muons detected by the detectors is proportional to the measurement duration. It affects the statistical fluctuations, which in turn impacts the reconstructed image quality. To investigate the reconstructed image quality under different measurement durations, we select data sets from the beginning of the simulation data in Section III, each corresponding to 7, 14, 30, 90, and 180 days of equivalent measurement time. The algorithm parameters are the same as those in Section III. The slices of the reconstructed images are shown in Fig. 11.

It can be observed that in the reconstructed image slices corresponding to measurement durations of 7 days and 14 days, there are severe artifacts between the chamber and the walls, particularly at the bottom of the reconstructed images. As the measurement duration exceeds 30 days, the artifacts are effectively suppressed, and the boundary between the chamber and the rammed earth becomes relatively clear. The reconstructed image slices for measurement durations of 90

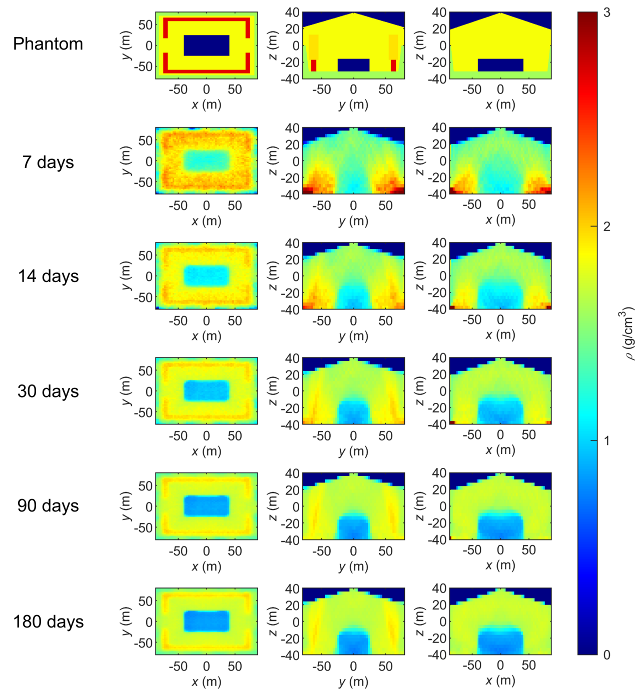

Fig. 11. Slices of the phantom and SIRT-TV reconstructed images for different equivalent measurement durations.

TABLE 3. $J_{\rm chamber}$ and $J_{\rm wall}$ of reconstructed images obtained using SIRT-TV under different equivalent measurement durations.

Time (day)	$J_{\rm chamber}$	$J_{\rm wall}$
7	0.2615	0.2050
14	0.4514	0.2465
30	0.5123	0.3383
90	0.5525	0.4994
180	0.5929	0.5498

days and 180 days are quite similar, with $J_{\rm chamber}$ and $J_{\rm wall}$ both $\gtrsim 0.5$, as can be seen in Table 3.

V. CONCLUSION

This paper conducts simulation research on 3D image reconstruction of muon tomography for a QinShiHuang tomb phantom using the SIRT-TV algorithm. The reconstructed image quality is evaluated based on the geometric similarity of structures. The results show that, compared to the SIRT algorithm, the SIRT-TV algorithm can effectively suppress salt-and-pepper artifacts. It improves the geometric similarity $J_{\rm chamber}$ by nearly one-third and $J_{\rm wall}$ by nearly twofold, and it converges faster. This suggests that SIRT-TV algorithm is more suitable for 3D image reconstruction of large-scale cultural heritage muon tomography. Using this algorithm with simulated 12-view cosmic-ray muon data, locations and shapes of the tomb chamber and walls are reconstructed. This study also investigated the impact of TV-minimization algorithm parameters on the reconstructed image quality by varying the maximum iteration number $N_{\rm TV}$ and the TV gradient descent step size α. The results indicate that, although the optimal TV parameters for walls reconstruction differ from those for tomb chamber reconstruction, selecting parameters within a reasonable range can achieve high-quality reconstructions. Considering the potential constraints in experiments, this paper also discusses the impact of measurement configurations and durations on the reconstruction results. The results show that reducing the number of views from 12 to 4 leads to a decrease in J. Among the three different 4-view configurations, the J values are highest when the detectors are positioned along the symmetry axes of the ROI. For the 12-view configuration, the J values steadily increase with the equivalent measurement duration, and both $J_{\rm chamber}$ and $J_{\rm wall} \gtrsim 0.5$ after an equivalent measurement duration of 90 days. These findings can provide guidance for selecting measurement configurations and durations for future experiments.

The reconstruction quality of SIRT-TV is substantially improved compared to SIRT, still, there is room for further enhancement: the two walls with different densities in the reconstructed image remain indistinguishable, and the geometric similarity J can also be improved. Future work could further enhance image quality, for example, by utilizing machine learning techniques. By simulating muon data from the QinShiHuang tomb phantom under varying viewpoints and equivalent measurement durations, the reconstructed images generated by the SIRT-TV algorithm can be used as inputs to train machine learning models, enabling further improvements in image quality.

While the QinShiHuang tomb phantom established in this study is a simplified phantom, it retains the essential structural features of the underground palace. As one of the most well-known imperial tombs in China, the structure of the QinShiHuang tomb is likely representative. Transmission muography simulation based on this tomb phantom would also provide insights for potential transmission muography experiments on other imperial tombs.

[1] P.A. Zyla, R.M. Barnett, J. Beringer, et al., Review of Particle Physics. Prog. Theor. Exp. Phys. **2020**, 083C01 (2020). doi: 10.1093/ptep/ptaa104

[2] K. Nagamine, M. Iwasaki, K. Shimomura, et al., Method of Probing Inner-Structure of Geophysical Substance with the Horizontal Cosmic-Ray Muons and Possible Application to Volcanic-Eruption Prediction. Nucl. Instrum. Methods Phys. Res. Sect. A-Accel. Spectrom. Dect. Assoc. Equip. **356**, 585-595 (1995). doi: 10.1016/0168-9002(94)01169-9

[3] H.K.M. Tanaka, H. Taira, T. Uchida, et al., Three-dimensional

computational axial tomography scan of a volcano with cosmic ray muon radiography. Journal of Geophysical Research: Solid Earth. **115**, 2010JB007677 (2010). doi: 10.1029/2010JB007677

[4] Y.P. Cheng, R. Han, Z.W. Li, et al., Imaging internal density structure of the Laoheishan volcanic cone with cosmic ray muon radiography. Nucl. Sci. Tech. **33**, 84-93 (2022). doi: 10.1007/s41365-022-01072-4

[5] H.K.M. Tanaka, H. Miyajima, T. Kusagaya, et al., Cosmic muon imaging of hidden seismic fault zones: Rainwater permeation into the mechanical fractured zones in Itoigawa–Shizuoka Tectonic Line, Japan. Earth Planet. Sci. Lett. **306**, 156-162 (2011). doi: 10.1016/j.epsl.2011.03.036

[6] S. Miyamoto, J. Barrancos, C. Bozza, et al., Muography of 1949 fault in La Palma, Canary Islands, Spain. Ann. Geophys. **60**, 9 (2017). doi: 10.4401/ag-7385

[7] K. Yamazaki, A. Taketa, D. Ikeda, et al., Development of detector and method for density structure measurement of fault zones using cosmic ray muons. Nucl. Instrum. Methods Phys. Res. Sect. A-Accel. Spectrom. Dect. Assoc. Equip. **1031**, 166518 (2022). doi: 10.1016/j.nima.2022.166518

[8] D. Bryman, J. Bueno, K. Davis, et al. Muon Geotomography-Bringing New Physics to Orebody Imaging. In: K.D. Kelley, H.C. Golden, (eds), *BUILDING EXPLORATION CAPABILITY FOR THE 21ST CENTURY*. pp. 235-241, SEG Conference on Keystone - Building Exploration Capability for the 21st Century (2014).

[9] D. Bryman, J. Bueno, J. Jansen, Blind Test of Muon Geotomography for Mineral Exploration. ASEG Extended Abstracts. **2015**, 1-3 (2015). doi: 10.1071/ASEG2015ab054

[10] D. Schouten, P. Ledru, Muon Tomography Applied to a Dense Uranium Deposit at the McArthur River Mine. Journal of Geophysical Research: Solid Earth. **123**, 8637-8652 (2018). doi: 10.1029/2018JB015626

[11] G.R. Liu, K.Q. Yao, F.Y. Niu, et al., Deep investigation of muography in discovering geological structures in mineral exploration: a case study of Zaozigou gold mine. Geophys. J. Int. **237**, 588-603 (2024). doi: 10.1093/gji/ggae057

[12] K. Morishima, M. Kuno, A. Nishio, et al., Discovery of a big void in Khufu's Pyramid by observation of cosmic-ray muons. Nature. **552**, 386-390 (2017). doi: 10.1038/nature24647

[13] L. Cimmino, G. Baccani, P. Noli, et al., 3D Muography for the Search of Hidden Cavities. Sci. Rep. **9**, 2974 (2019). doi: 10.1038/s41598-019-39682-5

[14] H.K.M. Tanaka, K. Sumiya, L. Oláh, Muography as a new tool to study the historic earthquakes recorded in ancient burial mounds. Geoscientific Instrumentation, Methods and Data Systems. **9**, 357-364 (2020). doi: 10.5194/gi-9-357-2020

[15] G.R. Liu, X.J. Luo, H. Tian, et al., High-precision muography in archaeogeophysics: A case study on Xi'an defensive walls. J. Appl. Phys. **133**, 14901 (2023). doi: 10.1063/5.0123337

[16] D. Borselli, T. Beni, L. Bonechi, et al., Muography as a support technique for non-invasive research and three-dimensional localization of tombs in archaeological sites: a case study from Palazzone Necropolis (Perugia – Italy). J. Instrum. **19**, C2076 (2024). doi: 10.1088/1748-0221/19/02/C02076

[17] H. Fujii, K. Hara, S. Hashimoto, et al., Performance of a remotely located muon radiography system to identify the inner structure of a nuclear plant. Prog. Theor. Exp. Phys. **2013**, 073C01 (2013). doi: 10.1093/ptep/ptt046

[18] K. Takamatsu, H. Takegami, C. Ito, et al., Cosmic-ray muon radiography for reactor core observation. Ann. Nucl. Energy. **78**, 166-175 (2015). doi: 10.1016/j.anucene.2014.12.017

[19] H. Fujii, K. Hara, K. Hayashi, et al., Investigation of the Unit-1 nuclear reactor of Fukushima Daiichi by cosmic muon radiography. Prog. Theor. Exp. Phys. **2020**, 043C02 (2020). doi: 10.1093/ptep/ptaa027

[20] J.M. Zhang, Z.W. Li, F. L, et al., Influence of multiple Coulomb scattering on accuracy of muon transmission imaging of small-scale matter. Acta Phys. Sin. **72**, 021401 (2023). doi: 10.7498/aps.72.20221792

[21] R. Nishiyama, Y. Tanaka, S. Okubo, et al., Integrated processing of muon radiography and gravity anomaly data toward the realization of high-resolution 3-D density structural analysis of volcanoes: Case study of Showa-Shinzan lava dome, Usu, Japan. Journal of Geophysical Research: Solid Earth. **119**, 699-710 (2014). doi: 10.1002/2013JB010234

[22] K. Jourde, D. Gibert, J. Marteau, Improvement of density models of geological structures by fusion of gravity data and cosmic muon radiographies. Geoscientific Instrumentation, Methods and Data Systems. **4**, 177-188 (2015). doi: 10.5194/gi-4-177-2015

[23] S. Nagahara, S. Miyamoto, K. Morishima, et al., Three-dimensional density tomography determined from multi-directional muography of the Omuroyama scoria cone, Higashi–Izu monogenetic volcano field, Japan. Bull. Volcanol. **84**, 94 (2022). doi: 10.1007/s00445-022-01596-y

[24] A. Barnoud, V. Cayol, P.G. Lelièvre, et al., Robust Bayesian Joint Inversion of Gravimetric and Muographic Data for the Density Imaging of the Puy de Dôme Volcano (France). Front. Earth Sci. **8**, 575842 (2021). doi: 10.3389/feart.2020.575842

[25] X.D. Jiang, W. Zhang, H. Yang. The research on Bayesian inference for geophysical inversion. Reviews of Geophysics and Planetary Physics. **53**, 159-171 (2022). doi: 10.19975/j.dqyxx.2021-042

[26] A Erlandson, K Boniface, V N P Anghel, et al. ONE-SIDED MUON TOMOGRAPHY—A PORTABLE METHOD FOR IMAGING CRITICAL INFRASTRUCTURE WITH A SINGLE MUON DETECTOR. CNL Nucl. Rev., **7**, (2018). doi: 10.12943/CNR.2016.00014

[27] S. Procureur, Muon tomography of large structures with 2D projections. Nucl. Instrum. Methods Phys. Res. Sect. A-Accel. Spectrom. Dect. Assoc. Equip. **1013**, 165665 (2021). doi: 10.1016/j.nima.2021.165665

[28] K. Hartling, F. Mahoney, E.T. Rand, et al., A comparison of algebraic reconstruction techniques for a single-detector muon computed tomography system. Nucl. Instrum. Methods Phys. Res. Sect. A-Accel. Spectrom. Dect. Assoc. Equip. **987**, 164834 (2021). doi: 10.1016/j.nima.2020.164834

[29] E.J. Candès, J. Romberg, T. Tao, Robust Uncertainty Principles: Exact Signal Reconstruction From Highly Incomplete Frequency Information. IEEE Trans. Inf. Theory. **52**, 489-509 (2006). doi: 10.1109/TIT.2005.862083

[30] E.J. Candès, J.K. Romberg, T. Tao, Stable signal recovery from incomplete and inaccurate measurements. Commun. Pure Appl. Math. **59**, 1207-1223 (2006). doi: 10.1002/cpa.20124

[31] D.L. Donoho, Compressed sensing. IEEE Trans. Inf. Theory. **52**, 1289-1306 (2006). doi: 10.1109/TIT.2006.871582

[32] E.Y. Sidky, C. Kao, X. Pan, Accurate image reconstruction from few-views and limited-angle data in divergent-beam CT. J. X-Ray Sci. Technol. **14**, 119-139 (2006).

[33] E.Y. Sidky, X. Pan, Image reconstruction in circular cone-beam computed tomography by constrained, total-variation minimization. Phys. Med. Biol. **53**, 4777-4807 (2008). doi:10.1088/0031-9155/53/17/021

[34] N. Su, Y.Y. Liu, L. Wang, et al., Muon radiography simula-

tion for underground palace of Qinshihuang Mausoleum. Acta Phys. Sin. **71**, 64201 (2022). doi: 10.7498/aps.71.20211582

[35] D.E. Groom, N.V. Mokhov, S.I. Striganov, MUON STOPPING POWER AND RANGE TABLES 10 MeV–100 TeV. Atom. Data Nucl. Data Tables. **78**, 183-356 (2001). doi: 10.1006/adnd.2001.0861

[36] N. Su, Y.Y. Liu, L. Wang, et al., A Comparison of Muon Flux Models at Sea Level for Muon Imaging and Low Background Experiments. Front. Energy Res. **9**, 750159 (2021). doi: 10.3389/fenrg.2021.750159

[37] R Gordon, R Bender, G T Herman, Algebraic reconstruction techniques (ART) for three-dimensional electron microscopy and x-ray photography. J. theor. Biol. **29**, 471-481 (1970). doi: 10.1016/0022-5193(70)90109-8

[38] P. Gilbert, Iterative methods for the three-dimensional reconstruction of an object from projections. J. Theor. Biol. **36**, 105-117 (1972). doi: 10.1016/0022-5193(72)90180-4

[39] S. Agostinelli, J. Allison, K. Amako, et al., Geant4—a simulation toolkit. Nucl. Instrum. Methods Phys. Res. Sect. A-Accel. Spectrom. Dect. Assoc. Equip. **506**, 250-303 (2003). doi: 10.1016/S0168-9002(03)01368-8

[40] S.Y. Liu (ed.), *Geophysical Exploration for the Underground Palace of Emperor Qin Shi Huang Mausoleum*. (Geological Publishing House, Beijing, 2005)

[41] D. Reyna, A Simple Parameterization of the Cosmic-Ray Muon Momentum Spectra at the Surface as a Function of Zenith Angle. (2006). doi: 10.48550/arXiv.hep-ph/0604145

[42] W.W. Ding, Y.Y. Liu, L. Wang, et al., Fast Simulation Study of Muon Absorption Radiography Based on Energy Loss Calculation. At. Energy Sci. Technol. **56**, 2765-2772 (2022). doi: 10.7538/yzk.2022.youxian.0509

[43] Z. Wang, A.C. Bovik, H.R. Sheikh, et al., Image quality assessment: from error visibility to structural similarity. IEEE Trans. Image Process. **13**, 600-612 (2004). doi: 10.1109/TIP.2003.819861